Development and Initial Validation of a Novel Smoothed-Particle Hydrodynamics-Based Simulation Model of Trabecular Bone Penetration by Metallic Implants

Sloan A. Kulper,[1] Christian X. Fang,[1] Xiaodan Ren,[2] Margaret Guo,[3] Kam Y. Sze,[4] Frankie K. L. Leung,[1] William W. Lu[1]

[1]LKS Faculty of Medicine, Department of Orthopaedics & Traumatology, The University of Hong Kong, China, [2]School of Civil Engineering, Tongji University, Shanghai, China, [3]School of Medicine, Stanford University, Menlo Park, California, [4]Faculty of Engineering, Department of Mechanical Engineering, The University of Hong Kong, China

Received 3 August 2017; accepted 31 August 2017
Published online in Wiley Online Library (wileyonlinelibrary.com). DOI 10.1002/jor.23734

ABSTRACT: A novel computational model of implant migration in trabecular bone was developed using smoothed-particle hydrodynamics (SPH), and an initial validation was performed via correlation with experimental data. Six fresh-frozen human cadaveric specimens measuring $10 \times 10 \times 20$ mm were extracted from the proximal femurs of female donors (mean age of 82 years, range 75–90, BV/TV ratios between 17.88% and 30.49%). These specimens were then penetrated under axial loading to a depth of 10 mm with 5 mm diameter cylindrical indenters bearing either flat or sharp/conical tip designs similar to blunt and self-tapping cancellous screws, assigned in a random manner. SPH models were constructed based on microCT scans (17.33 μm) of the cadaveric specimens. Two initial specimens were used for calibration of material model parameters. The remaining four specimens were then simulated in silico using identical material model parameters. Peak forces varied between 92.0 and 365.0 N in the experiments, and 115.5–352.2 N in the SPH simulations. The concordance correlation coefficient between experimental and simulated pairs was 0.888, with a 95%CI of 0.8832–0.8926, a Pearson ρ (precision) value of 0.9396, and a bias correction factor Cb (accuracy) value of 0.945. Patterns of bone compaction were qualitatively similar; both experimental and simulated flat-tipped indenters produced dense regions of compacted material adjacent to the advancing face of the indenter, while sharp-tipped indenters deposited compacted material along their peripheries. Simulations based on SPH can produce accurate predictions of trabecular bone penetration that are useful for characterizing implant performance under high-strain loading conditions. © 2017 Orthopaedic Research Society. Published by Wiley Periodicals, Inc. J Orthop Res

Keywords: trabecular bone trauma implant simulation

Osteoporotic fractures are experienced by half of women and one-quarter of men over 50 years of age,[1,2] requiring millions of fracture fixation devices each year.[3] The efficacy of internal fixation implants for the repair of osteoporotic fractures is largely dependent on their ability to maintain a secure and stable hold of trabecular bone during surgical reduction and healing. Implant cut-out is a common mode of failure in osteoporotic patients,[4] in which the implant tip pushes through the trabecular bone and into surrounding tissues, such as the adjacent joint cartilage.[5]

While prior studies have examined a variety of issues related to implant stability in trabecular bone including ease of implant insertion,[6,7] resistance to pull-out and loosening,[8] the utility of cement augmentation,[9] and the use of blade-type implants in low-density bone,[10–14] the relationship between implant tip geometry and resistance to trabecular bone penetration has not been thoroughly examined. Internal fixation implants, however, have been produced with a variety of tip designs without a robust body of evidence supporting their merits.

Grant sponsor: Hong Kong General Research Fund; Grant number: 172057/14; Grant sponsor: Hong Kong Innovation and Technology Fund; Grant number: ITS/171/15FP.
Correspondence to: Christian X. Fang (T: +852-2255-4654; F: +852-2817-4392; E-mail: cfang@hku.hk);
Xiaodan Ren (T: +86-21-6598-1505; F: +86-21-6598-0696; E-mail: rxdtj@tongji.edu.cn)

Any attempt to characterize the contribution of a design element to implant stability in trabecular bone is hindered by the fact that the basic mechanisms of implant failure and migration are poorly understood.[15–17] The behavior of implants migrating through porous, highly compressible cancellous bone material have few fundamental principles existing at present to aid in either the design or analysis.[18–20] Recent studies have shown that basic measures of bone quality such as mineral density and individual trabecular strength provide relatively weak predictions of internal fixation implant failure.[21,22] Simulation offers a promising alternative pathway to predicting implant performance, as it conserves more of the original morphological complexity of the bone being evaluated. While numerous studies simulating the compression of trabecular bone samples have reported accurate predictions under both low and high-strain conditions,[20,23,24] there have been a few simulation studies of implant failure in trabecular bone under high strain conditions.[24]

Recent work by Kelly et al.[25,26] has shown that simulation based on finite element method (FEM) can be used to accurately represent high-strain yield of ovine and bovine trabecular bone during compression with implant-like indenters when pressure-dependency is incorporated into the model. Mesh-based models such as FEM, however, still have some inherent limitations when representing the fragmentation of bone material and the displacement of fragments, both of which can occur during implant migration and

cut-out in trabecular bone.[27] The investigation of alternative simulation methods without such inherent limitations may provide gains in efficiency and accuracy when simulating such conditions.

One such alternative is a to take a particle-based approach to the simulation of bone tissue: Smoothed-particle hydrodynamics (SPH) models have been successfully used in other disciplines to model extremely high-strain scenarios like the stability of structural piles in loose soil,[28] and ballistic penetration.[29] Previously studies in orthopaedics using SPH have focused on different problem areas, such as cement infiltration.[30] Supporting the notion that a particle-based method may be suitable for simulating implant failure in trabecular bone, a recent study has shown that trabeculae behave like independent mechanical elements at high degrees of strain.[31]

We developed a novel SPH-based model that can be used to accurately simulate implant penetration in trabecular bone. We hypothesize that such a simulation may predict the penetration performance of two implant tip designs (flat or conical) in proximal femoral trabecular bone of variable density and strength. Exploring this possibility would provide the basis for further investigation into the usefulness of SPH models in scenarios of greater complexity.

The primary objective of the present study, therefore, was to: (i) establish the expected performance characteristics of two different implant tips geometries using mechanical in vitro penetration of human trabecular bone from the proximal femur; and (ii) to construct a novel SPH-based simulated penetration model of the human trabecular bone experiments and explore the level of agreement and correlation with mechanical findings.

MATERIALS AND METHODS

Compressive material penetration experiments were conducted using 5.0 mm diameter indenters with either sharp (conical) or flat profiled tip designs in human trabecular bone (Group (1) to establish reference force displacement scenarios for validation of simulation (Group (2). Force-displacement data (F-D) were recorded continuously by destructive compression of material to a depth of 10 mm for level of agreement and correlational analysis (Table 1).

Preparation of Human Trabecular Bone Specimens

Six fresh-frozen human cadaveric specimens were extracted from proximal femurs of female donors with a mean age of 82 years (range 75–90). Diagnostic X-rays (Ultrafocus 100, Faxitron Bioptics, LLC, AZ) were taken in the anteroposterior plane to exclude for lesions or foreign bodies. A surgical saw was used to remove a central block of trabecular bone measuring $10 \times 10 \times 20$ mm, cut parallel to the axis of the femoral neck. Each specimen had its orientation marked, and was wrapped with a 2.5 mm thick layer of epoxy resin putty such that the 10×10 mm surface corresponding to the distal end was left exposed for indentation testing (Fig. 1). Specimen size was in excess of the indentation spacing used by Hvid et al. in prior osteopenetration studies.[35,36]

Table 1. Grouping of all Penetration Tests

Group Number (Size)	Group
Group 1 ($n = 6$)	Human trabecular bone experiment—flat and sharp tip
Group 2 ($n = 6$)	Human trabecular bone simulation—flat and sharp tip

Each specimen was scanned via microCT at 17.33 μm resolution to provide a record of its structure in an undamaged state. MicroCT calibration was completed per the manufacturer's protocol using a phantom of hydroxyapatite. Morphometric analysis was performed using CT Analyzer v1.14.1.4 (Bruker Corporation, MA). Half of all specimens were randomly assigned flat-tipped indenters, and the remaining were assigned sharp-tipped indenters.

Mechanical Penetration Experimentation Setup

Indenters were fabricated from 5.0 mm diameter rods of 6061-T6 aluminum, selected for its radiolucency. A review of the literature[32] indicated that the yield strength and elastic modulus of the material (250 MPa and 70 GPa, respectively) would provide satisfactory rigidity given the stresses anticipated during the experiment. Rods were cut into 40 mm segments, and one end of each segment was precision lathed to add either a flat or sharp/conical tip (55° vertex angle) (Fig. 1), abstract cylindrical and conical forms approximating typical blunt, and self-tapping cancellous screws, respectively.[33] Finished indenters were mounted with tips facing vertically downward in a MTS 858 Mini Bionix (MTS, Inc., MN) hydraulic loading machine using a 2.5 kN load cell via a Jacobs chuck vise, with the rear face of each indenter fully supported during loading.

Each specimen was placed in a steel mounting frame supporting its bottom face, and M6 set screws supported the sides of the specimen with minimal force. The indenter was then advanced into the specimen at a slow constant rate of 0.5 mm/min (strain rate of 0.04%/s), similar to experiments from in the literature, in order to minimize viscoelastic disturbances.[25] Displacement reached 10 mm while recording the force (F) as a function of indenter displacement (D).

Based on a modified protocol from a similar recent study,[34] a microCT system (Bruker Skyscan 1076, Bruker Corporation) was used to document structural damage during penetration at 2 mm intervals (i.e., 2 mm, 4 mm, and so on). At each interval, specimens were held stationary for 10 min to allow for stress relaxation, then removed from the mounting frame and scanned at 17.33 μm resolution. Indenters were scanned along with the specimen, taking care not to disturb their positions or orientations relative to the bone specimens. Following microCT scanning, each specimen was returned to the mounting frame and the loading piston was moved downward at 0.01 mm/s until precisely reaching the prior displacement and testing was resumed. Following indentation and scanning, indenters were removed, cleaned, and inspected for signs of failure or wear.

Simulated SPH Penetration Model Setup

Penetration experiments of human trabecular bone were simulated using a smoothed particle hydrodynamics (SPH) model in ABAQUS 6.13 (Dassault Systèmes, France). SPH was selected as the basis for our model due to our interest in representing high-strain, crushing and fragmentation

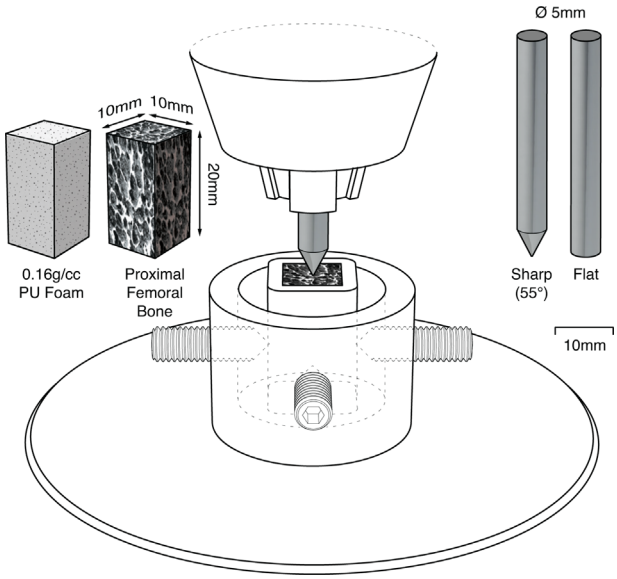

Figure 1. Illustration of indentation experiment setup.

damage behaviors of bone during compaction, and penetration. MicroCT scans of the six $10 \times 10 \times 20$ mm human trabecular bone specimens in their intact states were imported as uncompressed greyscale image stacks to construct 3D models. Minor rotational misalignments of these image stacks were corrected using DataViewer v1.5.2.4 (Bruker Corporation), and new volumes of interest (VOI) measuring $664 \times 664 \times 1264$ px were exported. VOIs were selected such that they included an approximately 1 mm thick layer of resin material on all sides in order to produce boundary conditions similar to the experiment. VOIs were then imported into CT Analyzer, and a thresholding function with a range of 75–255 was applied, corresponding to the approximate density of the trabeculae as confirmed by the hydroxyapatite phantom provided by the manufacturer. A pooling algorithm coded in Matlab R2016b v9.1 (The MathWorks, Inc., MA) was used to divide VOIs into numerous $8 \times 8 \times 8$ voxel groups. Groups with over 50% full voxels were then translated into SPH particle positions in a 3D matrix suitable for import into ABAQUS. This process thereby reduced the total particle count to less than 1.024×10^6 particles per specimen to strike a balance between accuracy and computing time (Fig. 2).

In ABAQUS, this SPH particle matrix data was then used to construct a 3D network of particles connected by mesh-free shape functions that determine their interactions per the degree of overlap. A material model with the properties below was applied to the SPH network in a manner consistent with the literature:[37] a softened elastoplastic model was adopted to reproduce the material nonlinearity of trabecular bone. The stress–strain law is defined as follows:

$$\boldsymbol{\sigma} = \mathbf{E} : (\boldsymbol{\varepsilon} - \boldsymbol{\varepsilon}^{\mathrm{p}}) \tag{1}$$

where $\boldsymbol{\sigma}$ is stress tensor; $\boldsymbol{\varepsilon}$ and $\boldsymbol{\varepsilon}^{\mathrm{p}}$ are strain and plastic strain, respectively; $\mathbf{E}$ is elasticity tensor. The associate evolution of plastic strain could be expressed as follows:

$$\begin{cases} \dot{\boldsymbol{\varepsilon}}^{\mathrm{P}} = \dot{\lambda} \dfrac{\partial f^{\mathrm{p}}(\boldsymbol{\sigma})}{\partial \boldsymbol{\sigma}} \\ f^{\mathrm{p}}(\boldsymbol{\sigma}) - r(k) = \sqrt{J_2} - r(k) \le 0 \\ \dot{k} = \sqrt{\dfrac{2}{3} \dot{\boldsymbol{\varepsilon}}^{\mathrm{P}} : \dot{\boldsymbol{\varepsilon}}^{\mathrm{P}}} \end{cases} \tag{2}$$

where J_2 is the second invariance of deviatoric stress $\mathbf{s}$. It is observed that the von Mises type yield function is defined in Equation (2). The hardening/softening function r(·) could be resolved by the uniaxial stress–strain relation. In the present work, the stress–strain relation under uniaxial loading is expressed in (Fig. 3):

CAD models of the indenters were imported into ABAQUS as rigid bodies. These simulated indenters were moved into the SPH bone network to a displacement depth of 10 mm while recording the required force. During loading, the specimen was fully constrained on the bottom surface, and the indenter was limited to movement along its main axis

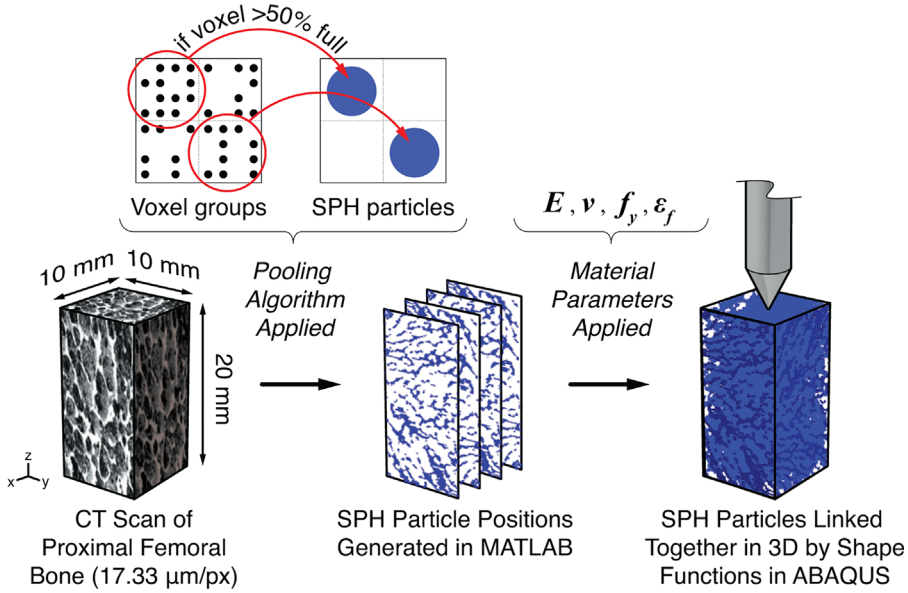

Figure 2. Preparation of simulated human trabecular bone specimen.

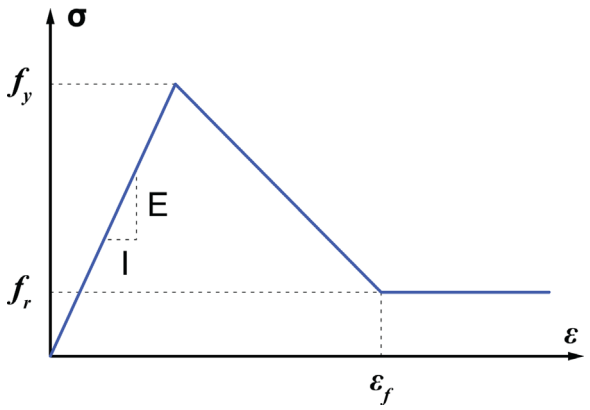

Figure 3. Uniaxial stress–strain relation.

(z-direction only). The coefficient of friction between indenter and simulated bone was 0.15.

A semi-blinded methodology was employed for simulation calibration. Two random specimens (No.1 and No.4) with different indenter tips were selected and used in repeated runs of the simulation to discover a set of material parameters capable of generating predicted F values until an average error of less than 20% was achieved. The resultant material parameter values (Table 2) were then uniformly applied to the simulation model for the remaining four specimens with no further calibration. Initial validation of the SPH model was conducted by correlating the six final simulated force-displacement curves with the experimental results.

STATISTICAL ANALYSIS

Force-displacement (F-D) data obtained from both mechanical experimentation (Group1) and simulation (Group2) were matched by D values. All D values were zeroed at a starting F value of 5 N to eliminate the initial "slack" effect in tests. Relaxation of bone material during microCT scans was shown in similar axial loading studies[32,34] to produce local dips in force values but to not affect the overall shape or maximum values of the F-D curve. These findings were confirmed in a pilot study (Supplementary Materials). Local dips in force values at 2 mm increments due to microCT scanning were therefore omitted from calculations of agreement between experimental and simulated results.

SPSS software v24.0 (IBM, Armonk, NY) and MedCalc software v17.6 (Ostend, Belgium) were used for statistical calculation. Minimum and maximum ranges (spread) in micro-CT morphometry values, and F for each group were expressed in descriptive terms. Spearman's rho two-tailed correlation coefficient was determined for pooled F values against bone density for each millimeter of penetration.

Agreement between the experimental and simulated F was determined by two methods. Firstly, a scatter plot between experimental and simulated F values was constructed and the concordance correlation coefficient determined as a product of the Pearson correlation coefficient and the bias factor as defined by Steichen and Cox[38] Secondly, a Bland and Altman[39] plot was constructed to determine the mean and the upper and lower bound 95% limits of agreement (LoA) between the two methods.

Table 2. Material Parameters of ABAQUS Model for Simulated Human Trabecular Bone

Material Model Parameter Values		
Young's Modulus	E	300 MPa
Poisson's Ratio	υ	0.3
Yielding stress	f_y	5 MPa
Fracture strain	ε_f	0.5
Residual stress	f_r	1 MPa

IMAGE ANALYSIS

Contour maps of the density changes in the human bone specimens following indenter penetration were generated using the Matlab R2016b Bioinformatics Toolbox. Prior to import in Matlab, pixels occupied by the indenters were deleted and image stacks were blurred (Gaussian, 20 px) to facilitate contour map generation using Photoshop CC2015.5 (Adobe, Inc, CA). MicroCT images used for figure display underwent filtering in DataViewer to facilitate viewing of mineralized bone compaction patterns; all images were inverted and their 8-bit greyscale ranges were adjusted to 51–150.

RESULTS

MicroCT densitometry revealed bone volume to total volume (BV/TV) ratio of specimens ranging from 17.88–30.49%. For the six experimental and simulation pairs (a total of 12), we obtained a total sample size of 5,345 data points. Force values showed high variation between the six simulated scenarios. Between samples, peak F measured by experimental method varied between 92.0 and 365.0 N, while peak F measured by SPH simulation varied from 115.5 to 352.2 N. The F measured at each 1 mm of displacement for each specimen is listed in Table 3. The pooled F values correlated significantly with CT morphometric bone density (BV/TV) from 3 to 8 mm ($p < 0.001$) with a correlation coefficient of 0.792–0.919 (strong correlation). Due to zeroing of the D = 0 values at F = 5 N, simulated F results were shifted forward and unavailable for analysis beyond 8 mm.

Analysis of microCT images of all six human trabecular bone specimens revealed consistent trends in the magnitude and location of bone compaction; penetration of the bone specimens by sharp indenters (Fig. 4, top row) resulted in density increases along the sides of the indenter penetration path, while the bone tissue directly beneath the indenter tip was generally unchanged. Conversely, penetration of bone specimens by flat indenters (Fig. 4, bottom row) demonstrated increases in density directly beneath the

Table 3. Detailed MicroCT Morphometry Data

	Micro CT Morphometrics					Force at Displacement (N)								
Specimen	BV/TV (%)	Tb.Sp (mm)	Tb.N ($1\,mm^{-1}$)	Tb.Th (mm)		1 mm	2 mm	3 mm	4 mm	5 mm	6 mm	7 mm	8 mm	9 mm	10 mm
1 – Flat	17.88	0.54	0.82	0.22	Experiment	58.3	57.1	56.3	84.5	91.0	72.9	71.8	68.4	80.6	84.0
					SPH Simul.	37.1	50.8	107.0	93.3	80.1	85.3	79.7	90.9	100.9	NA
2 – Flat	18.21	0.44	0.96	0.18	Experiment	67.9	57.9	70.5	67.4	73.6	75.4	76.4	78.8	75.4	71.4
					SPH Simul.	40.5	49.9	54.9	70.7	84.7	113.5	113.3	107.6	91.1	NA
3 – Flat	18.85	0.46	0.71	0.26	Experiment	52.4	51.2	61.6	77.3	99.7	82.6	90.0	92.2	89.2	102.8
					SPH Simul.	35.9	49.5	74.7	92.0	98.3	147.8	125.8	97.6	103.5	NA
4 – Sharp	26.63	0.4	1.1	0.24	Experiment	17.2	40.3	85.4	120.7	197.9	236.5	258.3	242.1	225.3	232.2
					SPH Simul.	11.9	34.7	116.0	266.1	295.5	295.0	283.5	282.6	NA	NA
5 – Sharp	27.9	0.3	1.41	0.19	Experiment	33.3	58.3	108.3	129.1	211.9	216.0	195.2	224.9	247.2	213.2
					SPH Simul.	24.7	97.5	202.7	268.3	279.5	278.1	270.3	NA	NA	NA
6 – Sharp	30.49	0.45	1.3	0.23	Experiment	38.9	123.2	191.8	246.2	265.2	321.3	296.0	262.3	237.5	232.3
					SPH Simul.	21.7	66.6	196.8	258.8	294.2	343.3	340.2	NA	NA	NA
Correlation with bone density BV/TV															
Correlation coefficient (Spearman's rho)						−.594*	.481	.792**	.749**	.848**	.891**	.919**	.847**	.768*	.886*
p value						.042	.114	.002	.005	.000	.000	.000	.002	.016	.019

Bone Volume (BV), Bone Volume/Total Volume (BV/TV), Trabecular Thickness (Tb.Th), Trabecular Spacing (Tb.Sp), Trabecular Number (Tb.N), Force measured per each 1 mm displacement and correlation between BV/TV and force for the pooled data. *Correlation is significant at the 0.05 level (two-tailed). **Correlation is significant at the 0.01 level (two-tailed).

indenter, with little to no change along the sides of the indenter penetration path.

Coronal slices of the simulated trabecular bone during indenter insertion revealed trends in the magnitude and location of bone compaction that were qualitatively similar to those of the experimental scenarios; penetration of the bone specimens by sharp indenters (Fig. 5) resulted in density increases along the sides of the indenter penetration path, while the bone tissue directly beneath the indenter tip was generally unchanged. Conversely, penetration of bone specimens by flat indenters (Fig. 6) resulted in increases in density directly beneath the indenter, with little to no change along the sides of the indenter penetration path. Videos of the simulated indentation of specimens No.4 (sharp) and No.1 (flat) were generated in ABAQUS to aid visualization of bone compaction (see Supplementary Materials) (Fig. 7).

Using all data from $D = 0$ onward, between the experimental and simulated groups, the concordance correlation coefficient is 0.888 (95%CI 0.883–0.893), Pearson ρ (precision) is 0.9396 (95%CI 0.9364–0.9427), and Bias correction factor Cb (accuracy) is 0.945, and significance level $p < 0.0001$. The Bland–Altman LoA is −20.94 N with 95% (1.96SD) lower and upper bound value between −94.81 and 52.93 N and the coefficient of repeatability was 84.5 with the simulated results biased towards an overestimation of F at higher values (Fig. 8).

DISCUSSION

The objective of this study was to validate the ability of a novel computational model of implant penetration in bone to accurately predict, and assist in mechanically characterizing, the performance of various implant tip designs in human trabecular bone of a range of quality. When conceiving of this study, care was taken to select tip designs that were both geometrically distinct and simple; distinctiveness being likely to produce a range of results conducive to rigorous testing of the simulation's accuracy, and simplicity being likely to facilitate interpretation of the data, given the present limitations in the understanding of the mechanisms of fracture and compaction in trabecular bone. A pilot study (described in Supplementary Materials) determined that flat tip designs and conical tips with a 55° vertex angle fit these criteria well. Indentation experiments were selected for their similarities to post-surgery physiological loading of an internal fixation implant.[34] Threads and other features were eliminated to isolate the mechanical contributions of the tip. Dimensions of the testing specimen and the indenter diameter were chosen based on similar prior osteopenetration studies[40,41] reporting that damage to trabecular bone was confined to a region of this size.

The cadaveric bone experiment established the following expectations for the results of the simulation: (i) tip design mainly affects the overall shape of the

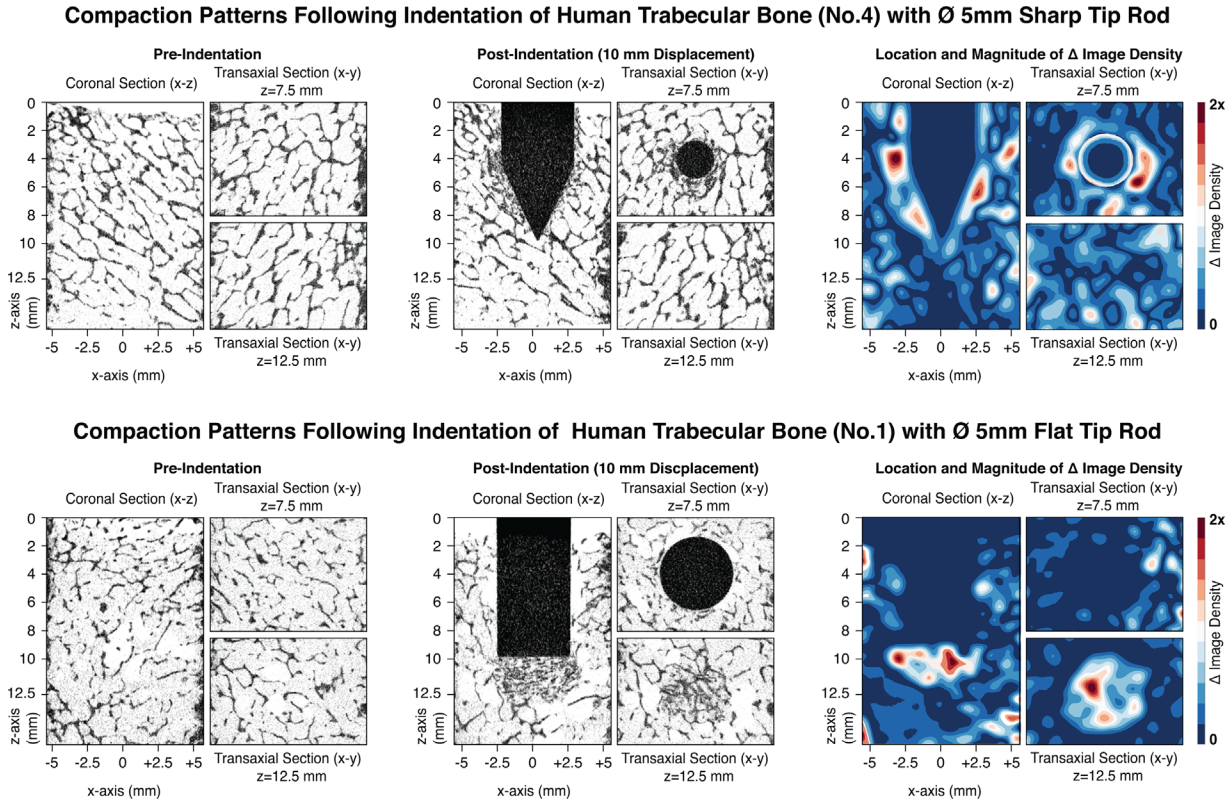

Figure 4. Compaction patterns following indentation of human bone specimens with sharp and flat-tipped rods demonstrated in Specimens No.4 (above) and No.1 (below).

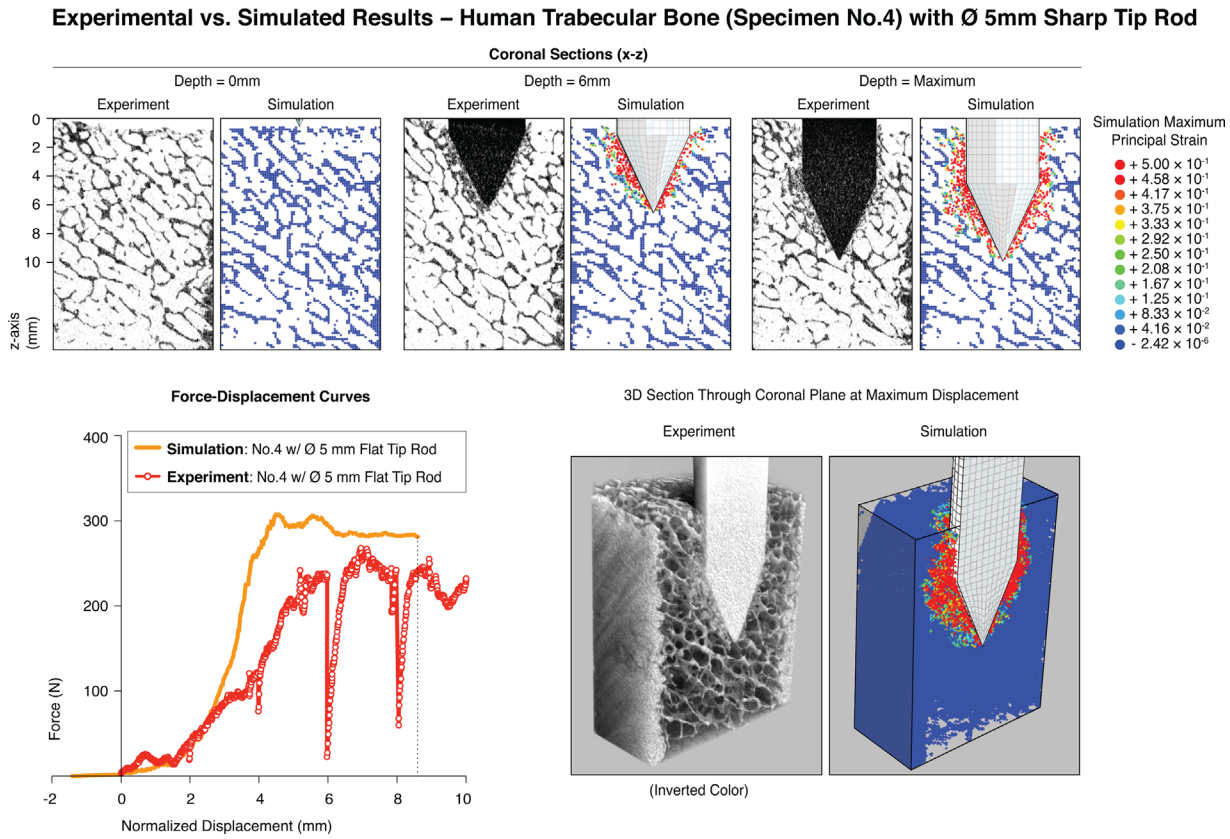

Figure 5. Experimental versus simulated results for specimen indented with sharp-tipped rod.

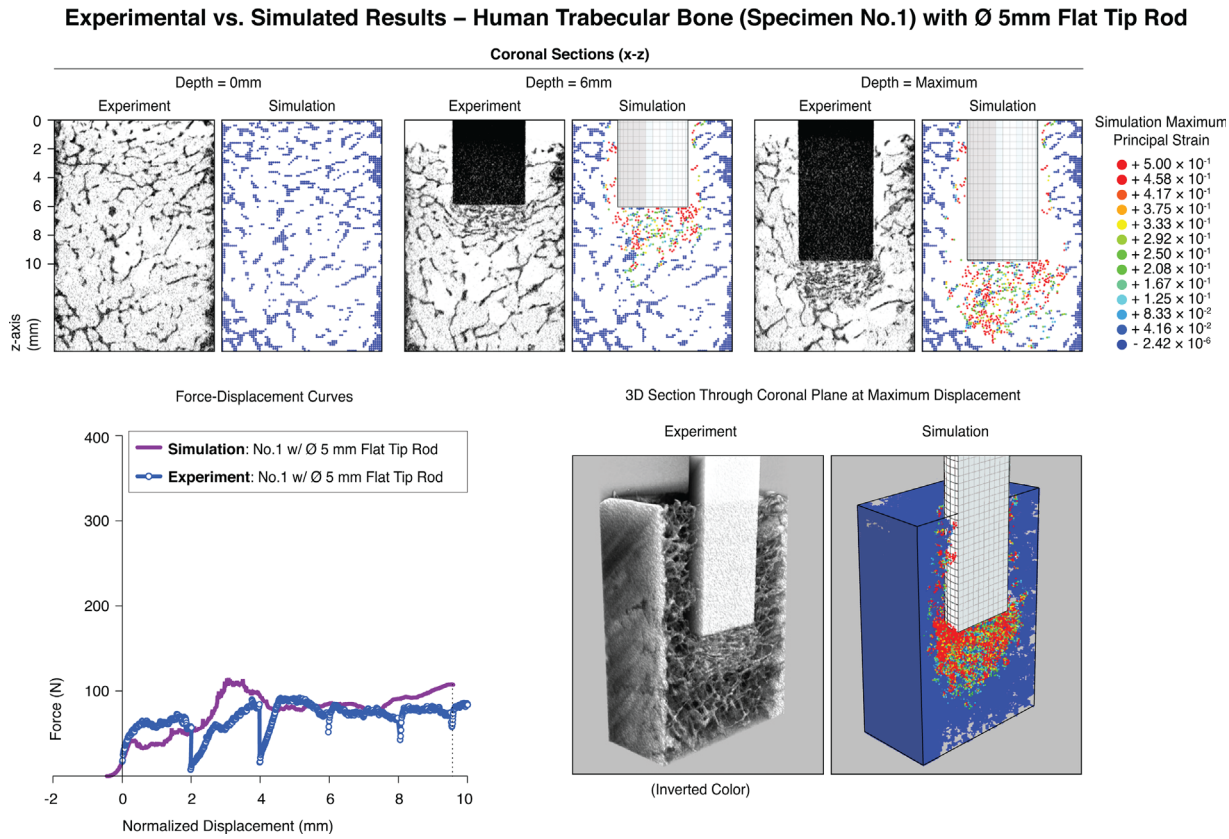

Figure 6. Experimental versus simulated results for specimen indented with flat-tipped rod.

force-displacement curve, with flat tips producing curves with initially steeper slopes that quickly flatten out, and sharp tips producing curves with slopes that gradually increase with displacement depth; while (ii) the density of the testing substrate mainly affects the magnitude of the displacement curve.

Distinct differences in compaction patterns were observed between tip designs, with flat tips generating a growing region of compacted material (referred to here as a bolus) directly below the tip, and sharp tips instead compacting material only along the sides of the indenter. Concentration of compacted material along the side of the indenter was consistent with the findings of similar push-in studies in polyurethane foam.[42] Large differences in density between human bone specimens, as well the extreme geometrical differences between tip designs, also provided a rigorous challenge for validation of the accuracy of the simulation. One drawback of the cadaveric experiment was its small sample size, which greatly reduced the overall computational burden of reproducing this experiment in silico, improving the feasibility of successfully completing and validating the simulation. This also, however, limited the usefulness of the cadaveric experiments in reaching definitive conclusions regarding the relative safety and efficacy of flat and sharp-tipped implants. Further study with a larger specimen sample set is needed to overcome this limitation.

The simulated indentation experiment demonstrated that particle-based modeling methods can be used to accurately predict key mechanical characteristics of implant-like indenters in trabecular bone under axial loading, when compared with experimental results: Force-displacement curve agreement was confirmed statistically, and patterns of bone compaction were qualitatively similar. The simulated results provided several insights into the characterization of implant tip performance in trabecular bone: (i) For flat indenters, relatively high levels of stress were observed among SPH particles in direct contact with the surface of the tip during initial loading, leading to high strain values as material in this region was crushed to form a dense bolus. Stress concentrations then shifted to two regions: The undamaged material directly below the bolus as well as a ring of material along its edge as this material was sheared away from the rest of the trabecular network. This suggests that the failure of flat-tipped implants under axial loading in trabecular bone may be described as the partial compaction and shearing-off of material directly below the tip surface, and the gradual accretion of this material into a dense cylindrical bolus of increasing length. The production of compacted bone extending beyond the end of the implant, as observed in the flat-tipped indenters, may be deleterious to implant performance; our findings suggest that in the case of cut-out due to loading along the axis of an implant, such a

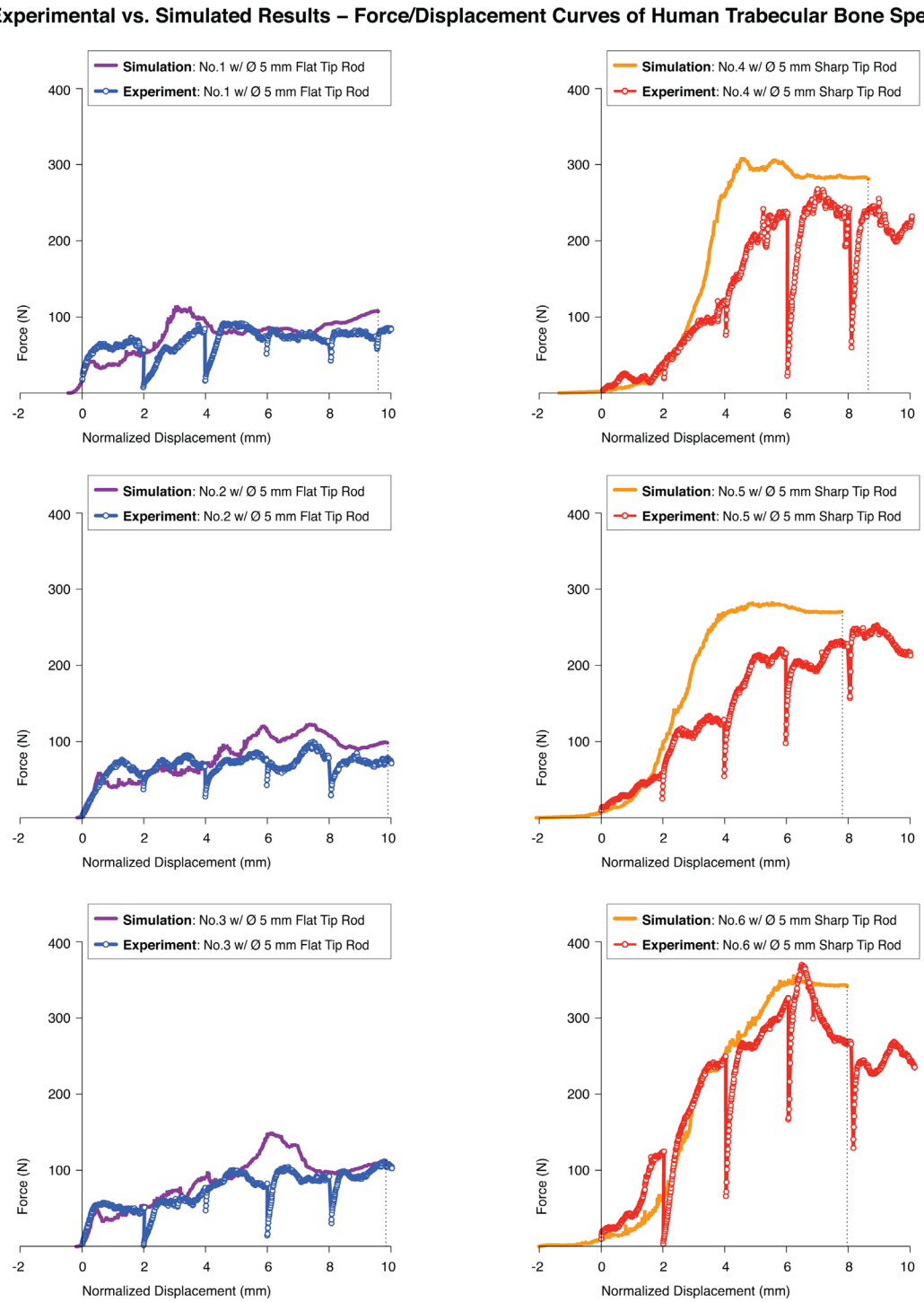

Figure 7. Force-displacement curves of human bone experiment-simulation pairs.

compacted bolus would begin to transmit stress to the subchondral and cortical layers of bone well in advance of the implant itself. Further investigation of the mechanical properties of the bolus created by flat-tipped indenters and its relationship to cut-out is needed and could provide the basis for more stable implant designs. (ii) Sharp-tipped indenters in both the real bone experiment and simulation, conversely, generated compacted material along their peripheries. Additionally, stress concentration was observed at the apexes of sharp-tips, where SPH particles were observed undergoing significant tensile stresses. This suggests that the failure of sharp-tipped implants under axial loading in trabecular bone may be characterized by a wedge-like mechanism whereby material is split apart from the center and partially crushed as it is pushed to the sides of the penetration path, where it is deposited in a compacted state.

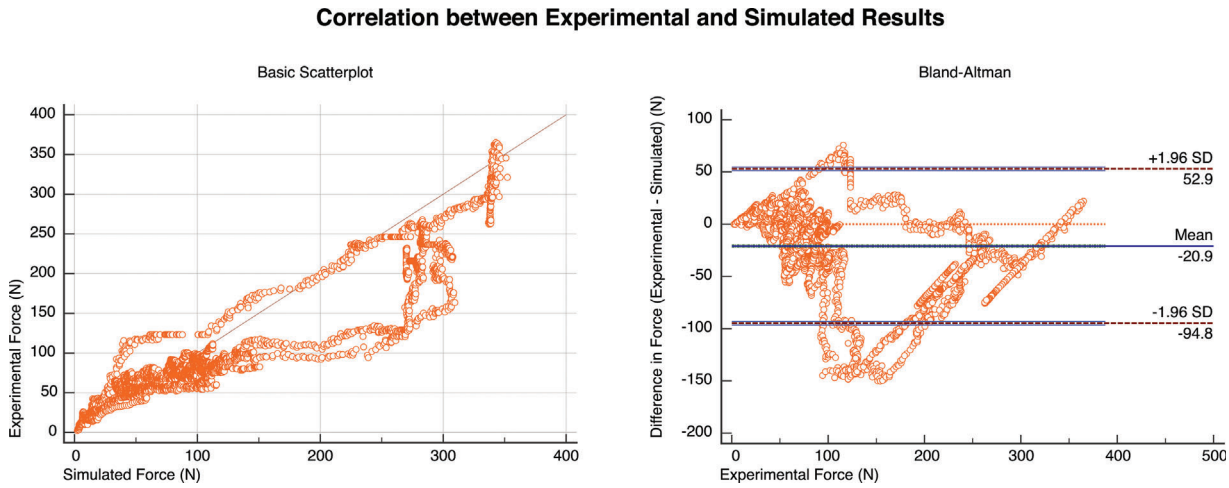

Figure 8. Graphs from statistical analysis of correlation between human bone experiment-simulation pairs (normalized).

Confirmation of the ability of the particle-based simulation model used in the current study to accurately predict scenarios beyond the current study, such as those with more complex implant geometries or loading conditions, will require additional research. The numerous intuitive advantages of simulation over destructive experiments for characterization of the mechanical performance of implant design features in trabecular bone include the abilities to repeat experiments in the same specimen of bone, and to reveal otherwise invisible patterns of mechanical stress and strain in a specimen. To our knowledge, this study represents the first time that penetration of trabecular bone has been successfully modeled with a particle-based simulation method such as SPH. Further study is required to explore the full range of utility of this method as a tool for investigating the mechanical behavior of trabecular bone in high strain conditions, and the performance of implants in this complex material.

AUTHORS' CONTRIBUTIONS

All authors contributed substantially to the experimental design and data interpretations, and have reviewed the final submitted manuscript. Sloan Kulper and Christian X. Fang designed and performed the experiments. Xiaodan Ren designed and developed the numerical models and ran the simulations. Sloan Kulper, Christian X. Fang, Xiaodan Ren, and Margaret Guo additionally contributed to data acquisition and manuscript drafting.

ACKNOWLEDGMENTS

We thank Professor Alfonso Ngan and Dr. Erica Ueda for their advice on the writing of the manuscript, and Mr. Stephen Chan, Ms. Jessica Kabigting, Ms. Minsoo Khan, Dr. Xu Lei, and Dr. Xiaoreng Feng, all of the University of Hong Kong, for their assistance running experiments during this study. Partial Grant support provided by Hong Kong General Research Fund grant 172057/14E and Hong Kong Innovation and Technology Fund grant ITS/171/15FP. Portions of the work presented here are patent-pending via The University of Hong Kong.

REFERENCES

1. WHO. 2004. Prevention and management of osteoporosis: WHO Technical Report. Available at: http://apps.who.int/.
2. NIH. 2000. Osteoporosis, prevention diagnosis and therapy: NIH Consensus Statement. Available at: Http://consensus.nih.gov/.
3. Johnell O, Kanis J. 2004. Epidemiology of osteoporotic fractures. Osteoporos Int 16:S3–S7.
4. Kanis JA, Odén A, McCloskey EV, et al. 2012. A systematic review of hip fracture incidence and probability of fracture worldwide. Osteoporos Int 23:2239–2256.
5. Simpson A, Varty K, Dodd C. 1989. Sliding hip screws: modes of failure. Injury 20:227–231.
6. Yerby S, Scott CC, Evans NJ, et al. 2001. Effect of cutting flute design on cortical bone screw insertion torque and pullout strength. J Orthop Trauma 15:216–221.
7. ASTM International. 2013. F543-13e1. Specification and test methods for metallic medical bone screws. Available at: http://www.astm.org/.
8. Goldhahn J, Reinhold M, Stauber M, et al. 2006. Improved anchorage in osteoporotic vertebrae with new implant designs. J Orthop Res 24:917–925.
9. Sermon A, Hofmann-Fliri L, Richards RG, et al. 2013. Cement augmentation of hip implants in osteoporotic bone: how much cement is needed and where should it go? J Orthop Res 32:362–368.
10. Siffri PC, Peindl RD, Coley ER, et al. 2006. Biomechanical analysis of blade plate versus locking plate fixation for a proximal humerus fracture: comparison using cadaveric and synthetic humeri. J Orthop Trauma 20:547–554.
11. Huang F-T, Lin K-C, Yang S-W, et al. 2012. Comparative study of the proximal femoral nail antirotation versus the reconstruction nail in the treatment of comminuted proximal femoral fracture. Orthopedics 35:e41–e47.
12. Wähnert D, Gudushauri P, Schiuma D, et al. 2010. Does cancellous bone compaction due to insertion of a blade implant influence the cut-out resistance? A biomechanical study. Clin Biomech 25:1053–1057.
13. Goffin JM, Pankaj P, Simpson AHRW, et al. 2013. Does bone compaction around the helical blade of a proximal femoral nail anti-rotation (PFNA) decrease the risk of cut-out?: a subject-specific computational study. Bone Joint Res 2:79–83.

14. Kold S, Rahbek O, Toft M, et al. 2005. Bone compaction enhances implant fixation in a canine gap model. J Orthop Res 23:824–830.
15. Dickenson RP, Hutton WC. 1981. The mechanical properties of bone in osteoporosis. J Bone Joint Surg Br 63:233–238.
16. Li B, Aspden RM. 1997. Composition and mechanical properties of cancellous bone from the femoral head of patients with osteoporosis or osteoarthritis. J Bone Miner Res 12:641–651.
17. Gefen A. 2002. Optimizing the biomechanical compatibility of orthopedic screws for bone fracture fixation. Med Eng Phys 24:337–347.
18. Gao H. 2006. Application of fracture mechanics concepts to hierarchical biomechanics of bone and bone-like materials. Int J Fract 138:101–137.
19. Gibson LJ. 1985. The mechanical behaviour of cancellous bone. J Biomech 18:317–328.
20. Ngan AHW. 2005. On the distribution of elastic forces in disordered structures and materials. I. Computer simulation. Proc R Soc Lond A: Math Phys Eng Sci 461:1423–1446.
21. Müller MA, Hengg C, Krettek C, et al. 2015. Trabecular bone strength is not an independent predictive factor for dynamic hip screw migration—a prospective multicenter cohort study. J Orthop Res 33:1680–1686.
22. Briot K, Paternotte S, Kolta S, et al. 2013. Added value of trabecular bone score to bone mineral density for prediction of osteoporotic fractures in postmenopausal women: the OPUS study. Bone 57:232–236.
23. Hussein AI, Barbone PE, Morgan EF. 2012. Digital volume correlation for study of the mechanics of whole bones. Procedia IUTAM 4:116–125.
24. Wirth AJ, Müller R, van Lenthe GH. 2010. Computational analyses of small endosseous implants in osteoporotic bone. Eur Cells Mater 20:58–71.
25. Kelly N, Harrison NM, McDonnell P, et al. 2012. An experimental and computational investigation of the post-yield behaviour of trabecular bone during vertebral device subsidence. Biomech Model Mechanobiol 12:685–703.
26. Kelly N, McGarry JP. 2012. Experimental and numerical characterisation of the elasto-plastic properties of bovine trabecular bone and a trabecular bone analogue. J Mech Behav Biomed Mater 9:184–197.
27. Clouthier AL, Hosseini HS, Maquer G, et al. 2015. Finite element analysis predicts experimental failure patterns in vertebral bodies loaded via intervertebral discs up to large deformation. Med Eng Phys 37:599–604.
28. Donz FV, Richefeu V, Magnier SA. 2009. Advances in discrete element method applied to soil, rock and concrete mechanics. Electron J Geotech Eng 1–44.
29. Liu MB, Liu GR. 2010. Smoothed particle hydrodynamics (SPH): an overview and recent developments. Arch Computat Methods Eng 17:25–76.
30. Basafa E, Murphy RJ, Kutzer MD, et al. 2013. A particle model for prediction of cement infiltration of cancellous bone in osteoporotic bone augmentation. PLoS ONE 8: e67958.
31. Wirth AJ, Müller R, Harry van Lenthe G. 2012. The discrete nature of trabecular bone microarchitecture affects implant stability. J Biomech 45:1060–1067.
32. Ryan MK, Mohtar AA, Cleek TM, et al. 2016. Time-elapsed screw insertion with microCT imaging. J Biomech 49:295–301.
33. Perren SM. 2002. Evolution of the internal fixation of long bone fractures. The scientific basis of biological internal fixation: choosing a new balance between stability and biology. J Bone Joint Surg Br 84:1093–1110.
34. Mueller TL, Basler SE, Müller R, et al. 2013. Time-lapsed imaging of implant fixation failure in human femoral heads. Med Eng Phys 35:636–643.
35. Hvid I, Andersen K, Olesen S. 1984. Cancellous bone strength measurements with the osteopenetrometer. Eng Med 13:73–78.
36. Hvid I, Hansen SL. 1985. Trabecular bone strength patterns at the proximal tibial epiphysis. J Orthop Res 3:464–472.
37. Ruffoni D, Müller R, van Lenthe GH. 2012. Mechanisms of reduced implant stability in osteoporotic bone. Biomech Model Mechanobiol 11:313–323.
38. Steichen TJ, Cox NJ. 2002. A note on the concordance correlation coefficient. Stata J 2.2:183–189.
39. Bland JM, Altman DG. 1999. Measuring agreement in method comparison studies. Stat Methods Med Res 8:135–160.
40. Jensen NC, Madsen LP, Linde F. 1991. Topographical distribution of trabecular bone strength in the human Os calcanei. J Biomech 24:49–55.
41. Frich L, Jensen N. 2014. Bone properties of the humeral head and resistance to screw cutout. Int J Shoulder Surg 8:21.
42. Kelly N, Cawley DT, Shannon FJ, et al. 2013. An investigation of the inelastic behaviour of trabecular bone during the press-fit implantation of a tibial component in total knee arthroplasty. Med Eng Phys 35:1599–1606.

SUPPORTING INFORMATION

Additional supporting information may be found in the online version of this article.